Supporting Information

Ionic Liquid Catalyzes Reactive CO_2 Capture

Rohan Sartape[1], Rashmi Mishra[2], Vamsi V. Gande[1], Sophia Johnson[1], Bianca Berry[3], Ishaku Amos[1], Rohit Chauhan[1], Amey Thorat[2], Jindal K. Shah[2], Meenesh R. Singh[1*]

[1] Department of Chemical Engineering, University of Illinois Chicago, 929 W. Taylor St., Chicago, Illinois, USA 60607

[2] School of Chemical Engineering, Oklahoma State University, Stillwater, Oklahoma, USA, 74078

[3] Lyons Township High School, Western Springs, IL 60558.

Corresponding Author

Meenesh R. Singh
Professor
Department of Chemical Engineering
929 W. Taylor St.
University of Illinois at Chicago
Chicago, IL 60607
Tel: (312) 996-3424
Email: mrsingh@uic.edu

S1. General Procedures

S1.1. Materials

ILs considered for the evaluation in this work were purchased from IOLITEC and were employed in the experiment without further purification. Additional information regarding the IL purity, abbreviation, molecular weight, mole fraction, and experimental conditions used are provided in **Table S1**. Pure ethylene glycol (EG) was obtained from Sigma Aldrich and dried in a vacuum oven at 60 °C for 12 hrs before use. Potassium hydroxide (KOH) of 99% purity, potassium bicarbonate ($KHCO_3$) of 99.9% purity, and silver (Ag) wire of 99% purity were obtained from Sigma Aldrich.

S1.2. Mixture preparation of IL and EG/KOH

Prior to the use of IL and EG in an experiment, the solutions were vacuum dried at 60 °C for 12 hrs, and the water content was determined in the solutions using a Metrohm Karl Fisher Titrator (EcoKF Titrator). It was ensured that the water content was less than 0.1% before each experiment. Later, KOH was dissolved in EG before the experiment. Calibration standards for determining the conductivity-based experiments of various concentrations of $KOH/KHCO_3$ were also prepared in a similar way, and the experiments were assigned as stock solutions. IL was mixed with stock solutions to evaluate the impact of IL on CO2 absorption rates. Typically, the mixture was prepared by adding aliquot samples of IL and stock solution in 2 ml microcentrifuge tubes. After the liquid dispensing step, the microcentrifuge tubes were held in a vortex mixer to thoroughly mix IL and the stock solution. A schematic illustration of the automated mixing of RTIL and EG is shown in **Figure S19.**

S1.3. Transient CO_2 absorption in IL and EG/KOH

A robotic hand-equipped electrochemical system was developed to study IL's transient CO2 capture kinetics. A custom electrode holder cell for conductivity measurement was 3D printed using Formlabs Form 3+ , which housed two silver electrodes (500 μm diameter) and a hypodermic needle for gas flow. 400 μL of the stock solutions were transferred into a 1 mL vial. A vial containing a solution along with electrodes acts as an electrolyte cell, and the cell constant was obtained by calibrating against the aqueous solution of KCl of 0.01 M, 0.1 M, 0.5 M, and 1 M concentration by the standard procedure.[1-3] Dobot Magician was used as a robotic hand to maneuver and place two electrodes at the same position in the vial for conductometric study. The ionic conductivity measurements were carried out by performing ZIR on a Biologic SP-300 potentiostat. All ZIR measurements were obtained at 298.15 K (unless stated) and performed on each binary mixture with a 20 mV sinusoidal pulse at 100 kHz.

In a typical experiment, the stock solutions were mixed with an aliquot amount of IL. After a uniform mixture was obtained, the samples were transferred to a vial. Calibration of the IL and EG/KOH system was determined by obtaining the resistance against the conductivity of the solution. A 10% CO_2 tank equipped with a CO_2 purifier was used to bubble at 10sccm inside the vial. For transient studies of CO_2 capture, the resistance of the solutions was obtained at specified time intervals by pausing the gas bubbling. The values obtained were then used to back-calculate the concentration of $KOH/KHCO_3$ using the previously obtained calibration of IL and EG/KOH. A similar protocol was also reported by our group previously.[4, 5] A 3M hollow fiber module was also utilized to validate the performance enhancement observed automated platform. The 3M hollow fiber module also known as 3M™ Liqui-Cel™ SP-0.5x1 has 1.7 ml and 1.0 ml capacity on the shell side and lumen side. The liquid was pumped through the peristaltic pump at 10 ml/min, while the gas flow rate was set to 5 ml/min. The conductivity of the CO2 capture solution (DES with and without IL) was continuously monitored by Thermo Scientific™ Orion™ DuraProbe™ Epoxy Bodied Graphite 4-Cell Conductivity Electrodes and measured via Thermo Scientific™ Orion Star™ A322 Conductivity Portable Meter. The feed gas was a mixture of 10% CO2 and the balance N_2 gas.

S1.4. Modelling pseudo-1st order reaction for CO_2 absorption kinetics

CO_2 capture kinetics of KOH dissolved in EG can be described as equation (**Sa**). Since the reaction is carried out in an organic medium devoid of water, the final product is in the bicarbonate form.[5] One of the simplest kinetic models that could describe the reaction would be a pseudo-first-order reaction, assuming the CO_2 concentration in the system remains constant. As shown in the rate equation (**Sb**), it can be simplified to equation (**Sc**), where k is the pseudo-first-order rate constant. Solving the differential equation (**Sd**) will lead to obtaining equation (**Se**), which can be used to obtain the rate constant, k, by linear regression. C_{OH^-} and $C^o_{OH^-}$ would be the hydroxide concentration at any point of time and initial hydroxide concentration in the system.

$$CO_2 + OH^- \rightarrow HCO_3^- \quad \text{(Sa)}$$

$$-r_{OH^-} = k' C_{CO_2} C_{OH^-} \quad \text{(Sb)}$$

$$-r_{OH^-} = k C_{OH^-} \text{ , where } k = k' C_{CO_2} \quad \text{(Sc)}$$

$$\frac{dC_{OH^-}}{dt} = k C_{OH^-} \quad \text{(Sd)}$$

$$\ln C_{OH^-} = -kt + C^o_{OH^-} \quad \text{(Se)}$$

For Arrhenius analysis, the rate constants were determined at 313, 323, and 333 K by performing linear regression on Equation **Se** for the initial 2 minutes of experimental data.

S1.5. Nuclear Magnetic Resonance (NMR)

All NMR spectra were acquired at 298.15 K (25 °C) using a Bruker DRX500 spectrometer. For each sample, ^{1}H NMR spectra were recorded with 16 scans and ^{13}C NMR spectra were collected with 128 scans, ensuring sufficient signal-to-noise ratio for quantitative comparison. Samples were prepared in DMSO-d6 as the lock solvent and were equilibrated for 10 minutes at room temperature prior to measurement to ensure thermal and chemical stability. Chemical shifts are reported in parts per million (ppm) relative to the residual solvent peak.

S1.6. IR measurements

In situ ATR-FTIR spectroscopy measurements were conducted using a Bruker Invenio-S FTIR spectrometer. Samples were deposited on a ZnSe crystal after background correction. Each spectrum was collected with 32 scans and was recorded at a resolution of 2 cm^{-1} using a liquid nitrogen-cooled, mid-band mercury cadmium telluride (MCT) detector.

S1.7. Surface Tension measurements

Surface tension measurements were carried out using a DCAT 25 dynamic contact angle and tensiometer system equipped with a platinum Wilhelmy plate. Prior to each measurement, the plate was thoroughly cleaned with ethanol and flame-treated to ensure complete wettability. The sample was placed in a temperature-controlled glass vessel and equilibrated for 5 minutes at room temperature (25 ºC) before each measurement.

S1.7. Quantum chemical calculations

To confirm and support the experimental observations, quantum chemical calculations were performed. All geometries were optimized using Gaussian 16[6] at B3LYP/6-311++G(d,p) level[7] with EG as the implicit solvent. Grimme's D3 dispersion correction[8] with Becke-Johnson (BJ) damping[9] was included to account for dispersion interactions. The solvent environment of EG was modeled using Integral Equation Formalism Polarizable Continuum Model (IEF-PCM)[10] with a dielectric constant (ε) of 37. The optimized geometries were then used to

calculate NMR spectra using Gauge-Independent Atomic Orbital (GIAO)[11-13] method, employing B3LYP/6-311+g(2d,p) and incorporating solvent effects of DMSO-d6 (ε =46.7) via IEF-PCM. Tetramethylsilane (TMS) at the B3LYP/6-311+G(2d,p) level was used as the reference for chemical shifts. The optimized geometries in EG as implicit solvent were used to simulate the IR spectra. Scaling was performed using the wavenumber-linear scaling (WLS) method to account for neglected anharmonic effects, align theoretical results with experimental data, and correct systematic errors to improve spectral accuracy. [14-16]

Table S1 RTILs structures, abbreviation, viscosity of neat RTILs and purity information; all samples were used without further purification.

IL structure	RTILs compound name	Abbreviation	CAS No.	Purity (wt.%)
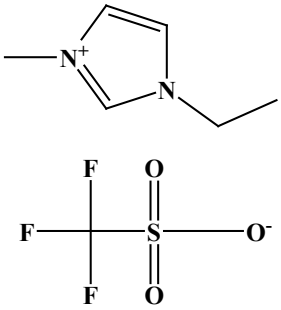	1-Ethyl-3-methylimidazolium trifluoromethanesulfonate/Triflate	EMIM OTf	145022-44-2	>99%
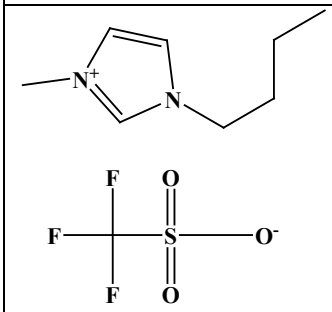	1-Butyl-3-methylimidazolium trifluoromethanesulfonate/Triflate	BMIM OTf	174899-66-2	>99%
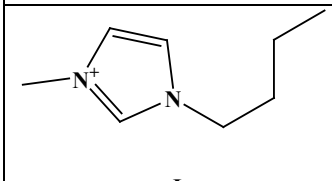	1-Butyl-3-methylimidazolium iodide	BMIM I	65039-05-6	>98%
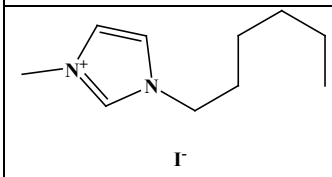	1-Hexyl-3-methylimidazolium iodide	HMIM I	178631-05-5	>98%
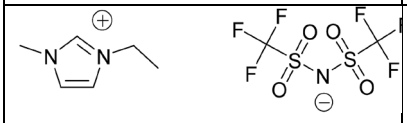	1-Ethyl-3-methylimidazolium bis(trifluoromethylsulfonyl)imide	EMIM NTf_2	174899-82-2	>98%
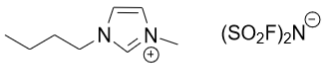	1-Butyl-3-methylimidazolium bis(trifluoromethylsulfonyl)imide	BMIM NTf_2	174899-83-3	>98%
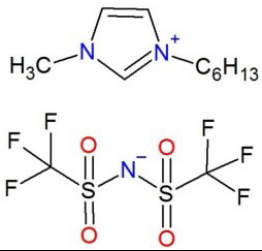	1-Hexyl-3-methylimidazolium bis(trifluoromethylsulfonyl)imide	HMIM NTf_2	382150-50-7	>98%
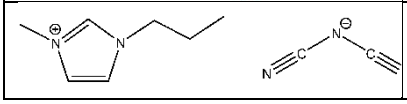	1-Butyl-3-methylimidazolium dicyanamide	BMIM DCA	448245-52-1	>98%

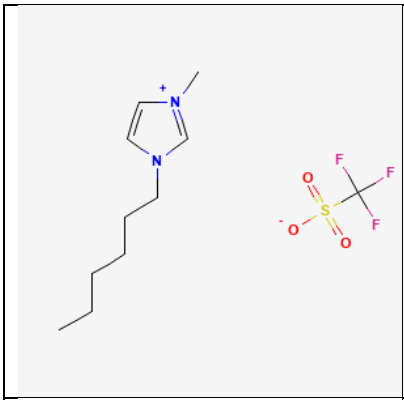	1-Hexyl-3-methylimidazolium trifluoromethanesulfonate/Triflate	HMIM OTf	460345-16-8	>99%
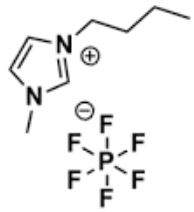	1-Butyl-3-methylimidazolium hexafluorophosphate	BMIM PF_6	174501-64-5	>98%
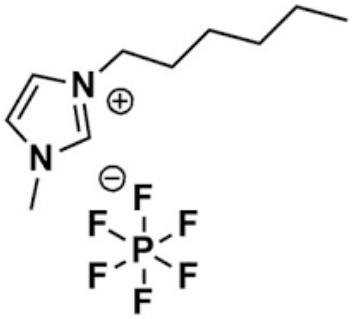	1-Hexyl-3-methylimidazolium hexafluorophosphate	HMIM PF_6	304680-35-1	>98%
Solvent				
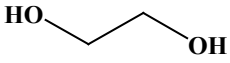	Ethylene glycol	EG	107-21-1	>99%

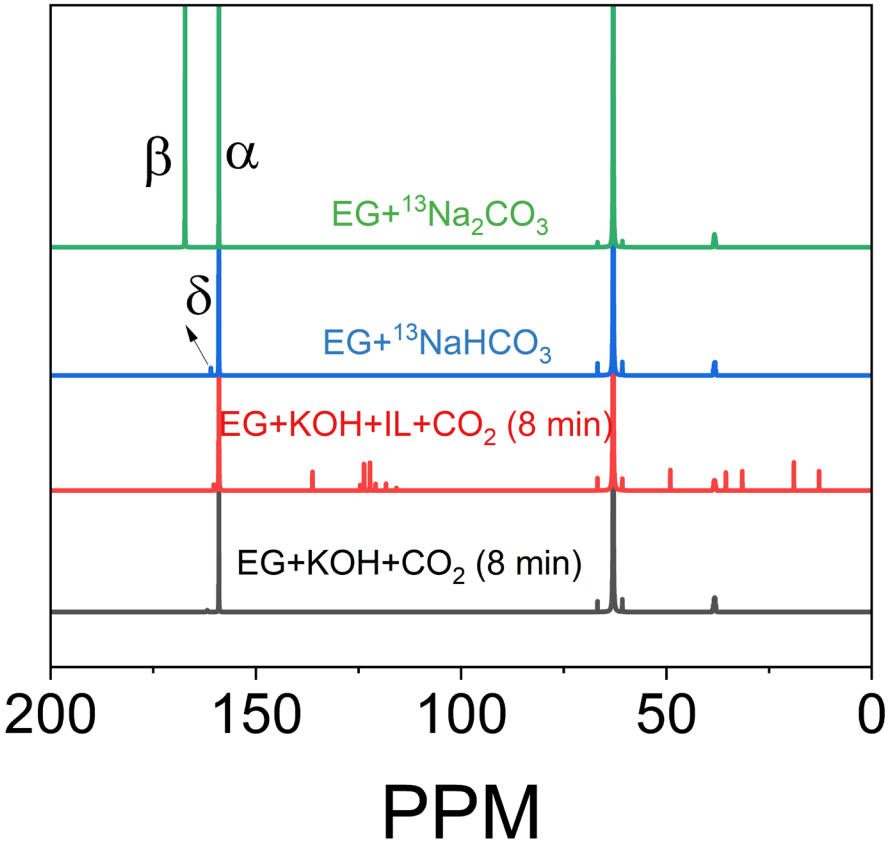

Figure S1. Comparison of ^{13}C NMR spectra of the samples containing $^{13}Na_2CO_3$, $^{13}NaHCO_3$, DES, and DES+IL. Peaks at 159 and 167 PPM, marked as α and β, respectively, confirm the bicarbonate and carbonate species formed during the CO2 bubbling experiment. A peak at 160.9 PPM marked as δ indicates the formation of the carbonate of ethylene glycol. IL is BMIM NTf_2 at a mixed volume percentage of 5%. All experiments were conducted at 298 K, with an initial concentration of 0.1 M KOH to compare the influence of IL.

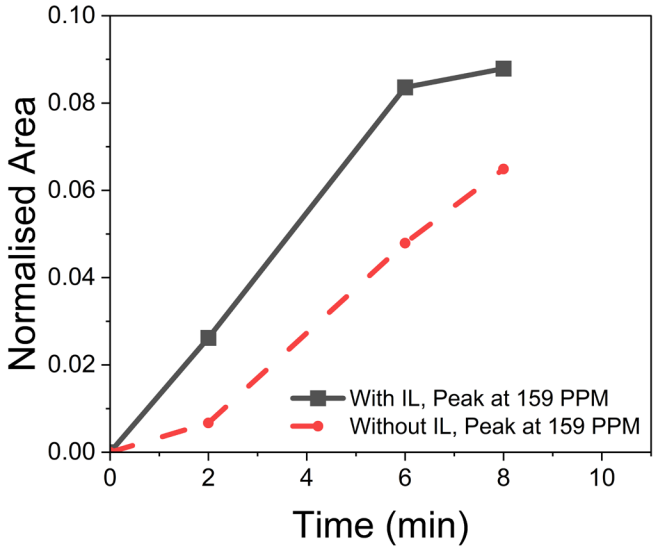

Figure S2. Comparison of NMR peak area at 159 PPM for the system with and without IL during the CO2 chemisorption experiment.

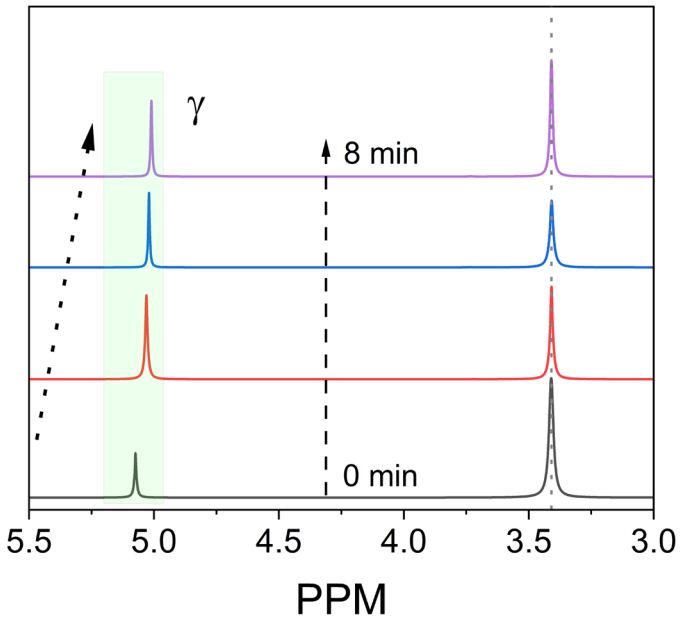

Figure S3. Upfield shift in ^{1}H NMR indicated by the arrow at 5.1 PPM, labelled without IL, indicating the water formation during CO_2 bubbling in the system from 0 to 8 minutes.

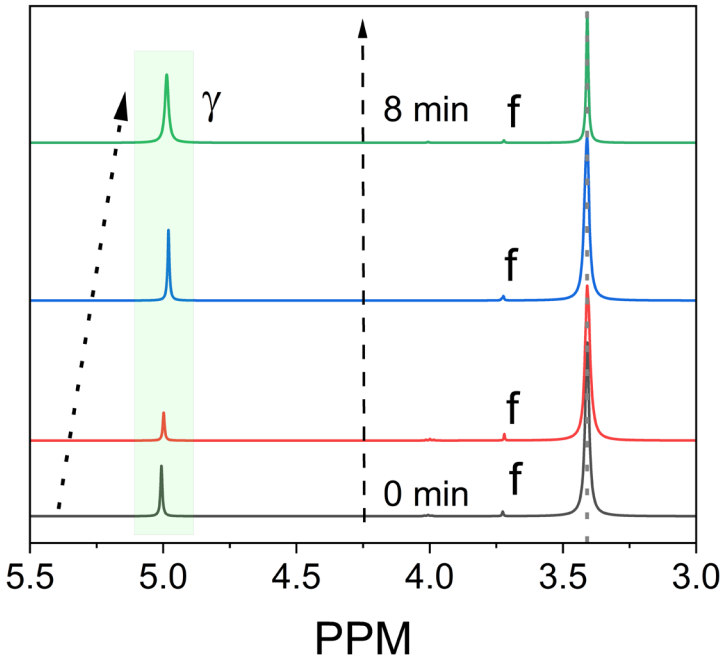

Figure S4. Upfield shift in ^{1}H NMR indicated by the arrow at 5.1 PPM, labelled with IL, indicating the water formation during CO_2 bubbling in the system from 0 to 8 minutes.

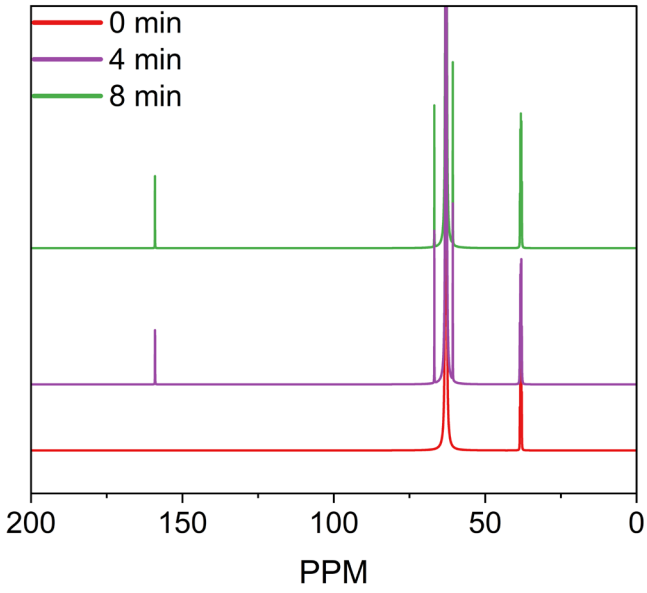

Figure S5. ^{13}C NMR spectra at different time intervals without IL by bubbling CO_2 containing flue gas. NMR peak at 159 PPM indicates the formation of bicarbonate in the system. All experiments were conducted at 298 K, with an initial concentration of 0.1 M KOH. The feed gas consists of 12.2 % CO_2, 0.16% SO_2, 7% O_2, and 80.2% N_2.

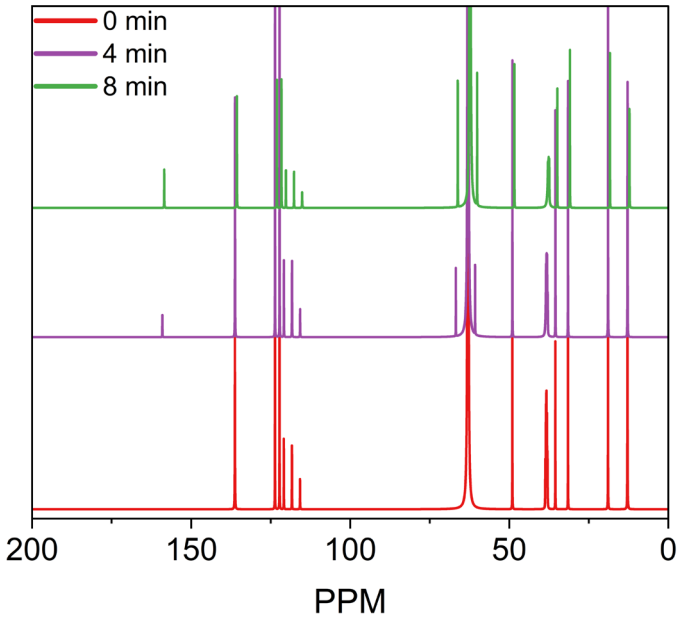

Figure S6. ^{13}C NMR spectra at different time intervals with IL by bubbling CO_2 containing flue gas. NMR peak at 159 PPM indicates the formation of bicarbonate in the system. IL is BMIM NTf_2 at a mixed volume percentage of 5%. All experiments were conducted at 298 K, with an initial concentration of 0.1 M KOH to compare the influence of IL. The feed gas consists of 12.2 % CO_2, 0.16% SO_2, 7% O_2, and 80.2% N_2.

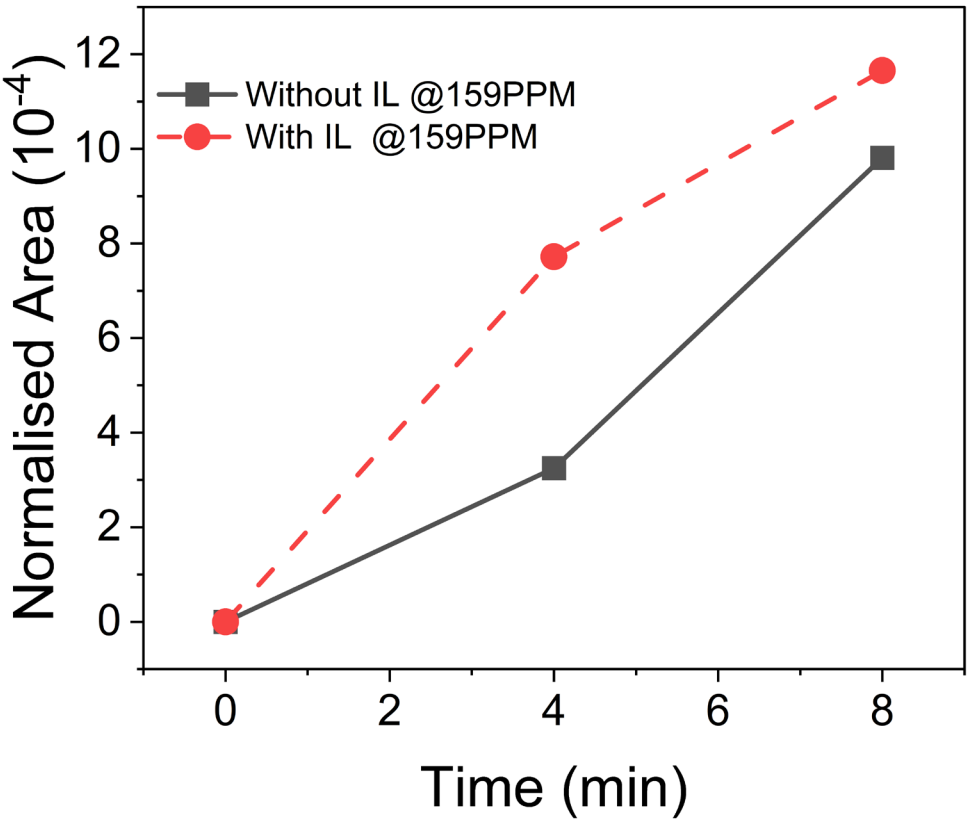

Figure S7. Comparison of ^{13}C NMR peak area at 159 PPM for the system with and without IL during the flue gas bubbling experiment. IL is BMIM NTf_2 at a mixed volume percentage of 5%. All experiments were conducted at 298 K, with an initial concentration of 0.1 M KOH to compare the influence of IL. The feed gas consists of 12.2 % CO_2, 0.16% SO_2, 7% O_2, and 80.2% N_2.

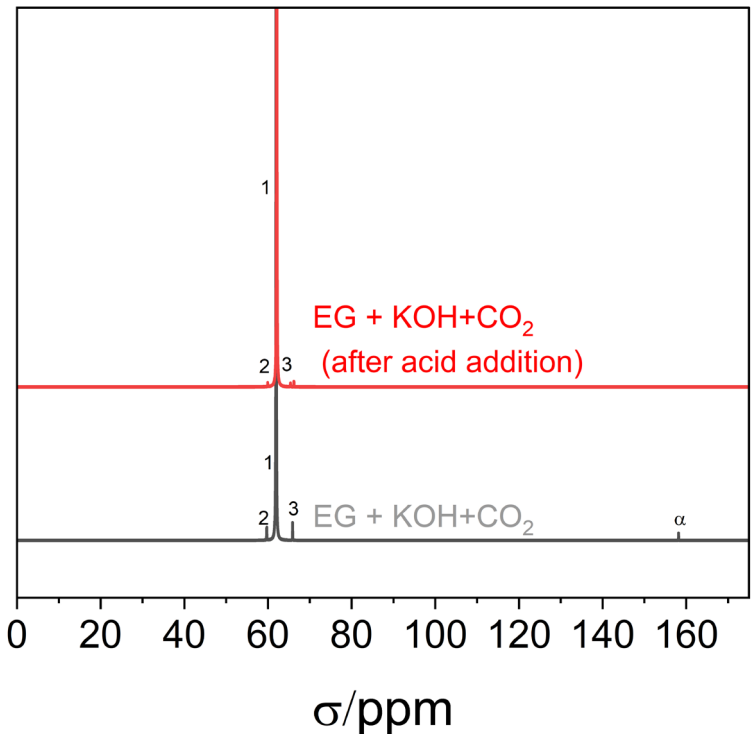

Figure S8. ^{13}C NMR spectra of the DES system in the presence of CO_2 and after acid addition.

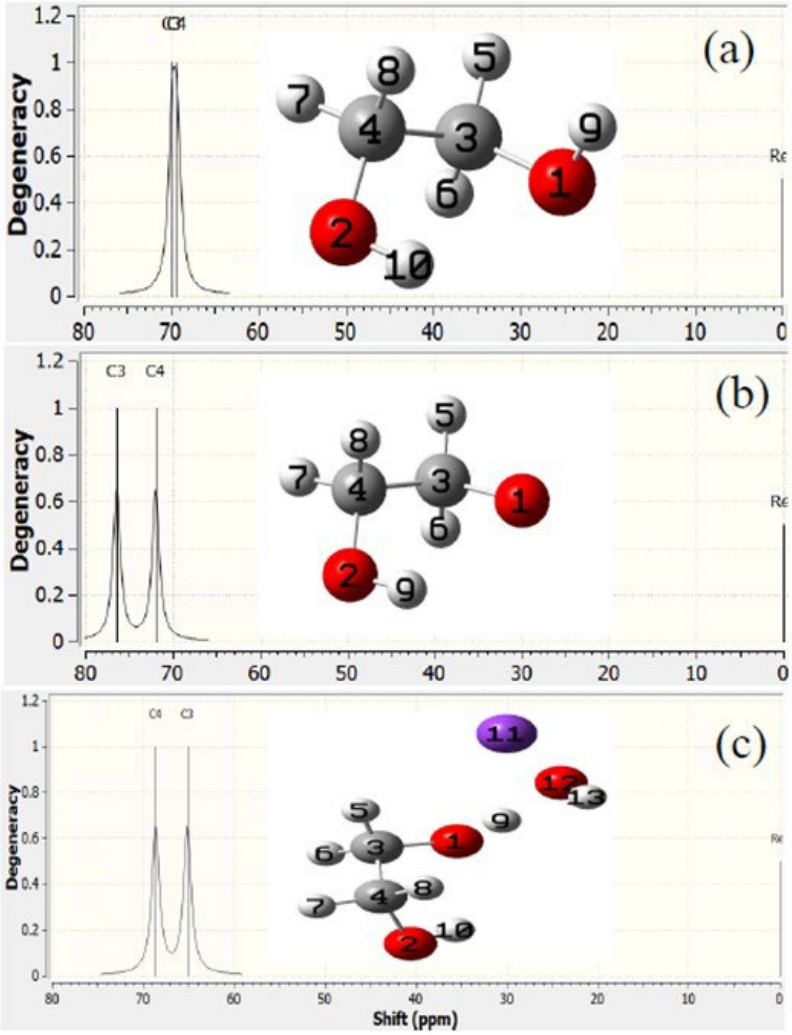

Figure S9. Comparison of simulated ^{13}C NMR spectra for (a) ethylene glycol (EG), (b) deprotonated ethylene glycol (EG^{-}), and (c) ethylene glycol deprotonated by KOH (EG + KOH). Atom colors: red = O, grey = C, white = H.

Table S2. A comparison of chemical shifts of ^{13}C NMR

Atom	**δ_calc (ppm)**			**δ_calc (ppm)**
	EG	**EG^{-}**	**EG+KOH**	**EG+KOH+CO_2**
C3	69.8538	76.4172	65.1286	67
C4	69.3062	71.9413	68.6142	68

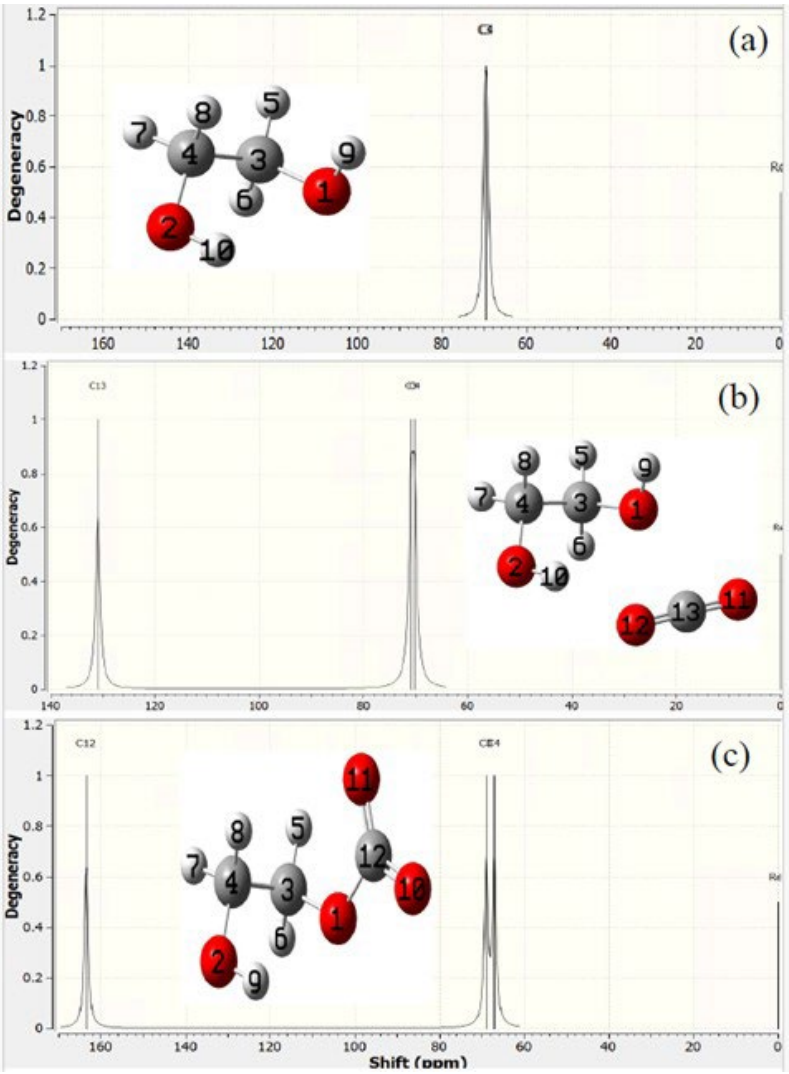

Figure S10. Comparison of simulated 13C NMR spectra for (a) ethylene glycol (EG), (b) physisorption of CO_2 by EG (EG+CO_2_P), and (c) chemisorption of CO_2 by EG (EG+CO_2_C). Atom colors: red = O, grey = C, white = H

Table S3. A comparison of chemical shifts of ^{13}C NMR

EG		**EG+CO_2_P**		**EG+CO_2_C**	
Atoms	**δ_calc (ppm)**	**Atoms**	**δ_calc (ppm)**	**Atoms**	**δ_calc (ppm)**
C3	69.8538	C3	68.9268	C3	70.8858
C4	69.3062	C4	67.0414	C4	70.2072
		C12	163.4712	C13	130.9051

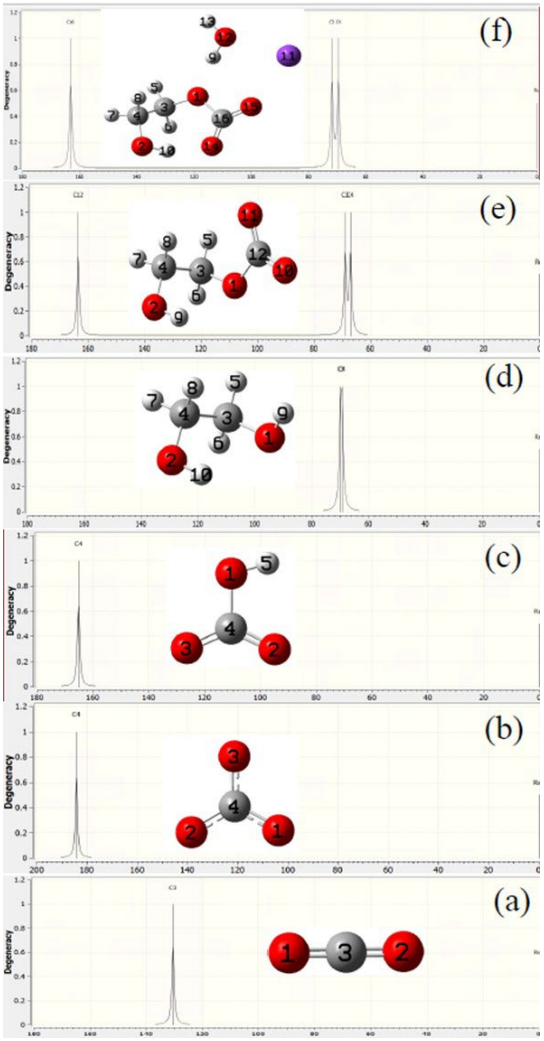

Figure S11. Comparison of simulated 13C NMR spectra for (a) carbon dioxide (CO_2), (b) carbonate (CO_3^{2-}), (c) bicarbonate (HCO_3^-), (d) ethylene glycol (EG), (e) hydroxyethyl carbonate ($EG^- + CO_2$), and (f) formation of hydroxyethyl carbonate and water upon CO_2 absorption by deprotonated EG (EG + KOH + CO_2). Atom colors: red = O, grey = C, white = H, purple = K.

Table S4. A comparison of chemical shifts of ^{13}C NMR

CO_2		**CO_3^{2-}**		**HCO_3^-**		**EG**		**EG^-+CO2**		**EG+KOH+CO_2**		**EG+KOH+CO_2**
Atoms	**δ_calc (ppm)**	**Atoms**	**δ_calc (ppm)**	**Atoms**	**δ_calc (ppm)**	**Atoms**	**δ_calc (ppm)**	**Atoms**	**δ_calc (ppm)**	**Atoms**	**δ_calc (ppm)**	**δ_exp (ppm)**
C3	130.4685	C4	184.1637	C4	165.1166	C3	69.8538	C3	68.9268	C3	71.7434	61
						C4	69.3062	C4	67.0414	C4	69.5481	67
								C16	163.4712	C16	163.1183	160.9

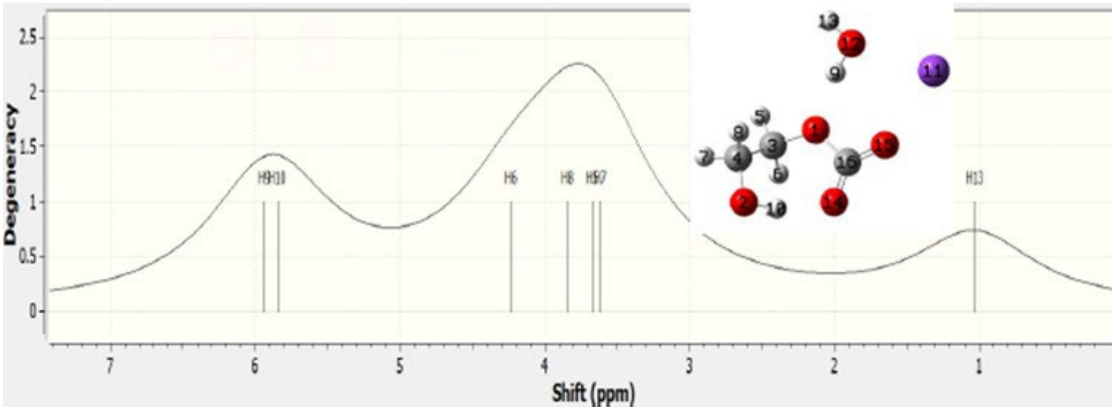

Figure S12. Simulated ^{1}H NMR spectra showing the formation of hydroxyethyl carbonate and water upon CO_2 absorption by deprotonated EG in the EG + KOH system (EG + KOH + CO_2). Atom colors: red = O, grey = C, white = H, purple = K.

Table S5. A comparison of chemical shifts of ^{13}C NMR

Atom	**δ_calc (ppm)**
	EG+KOH+CO_2
H9	5.9354
H10	5.8444
H6	4.2295
H8	3.8412
H5	3.6675
H7	3.6168
H13	1.0269

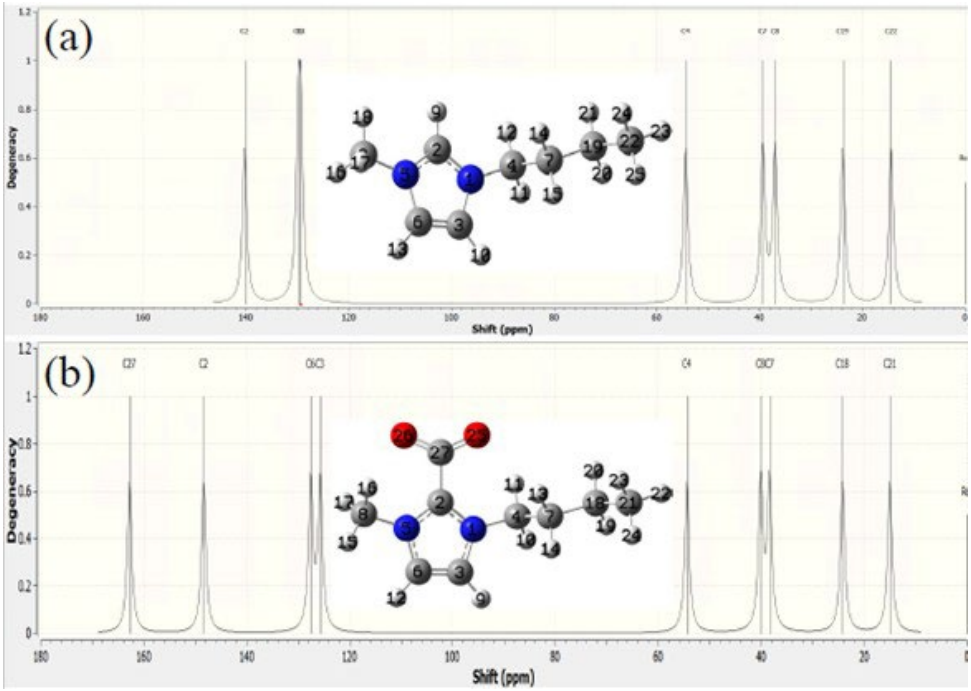

Figure S13. Comparison of simulated ^{13}C NMR spectra for (a) 1-butyl-3-methylimidazolium cation ($BMIM^+$) and (b) CO_2 chemisorbed by deprotonated $BMIM^+$. Atom colors: red = O, grey = C, white = H, blue = N.

Table S6. A comparison of chemical shifts of ^{13}C NMR

$BMIM^+$		**$BMIM^+$+CO2**	
Atoms	**δ_calc (ppm)**	**Atoms**	**δ_calc (ppm)**
C2	140.2523	C2	148.3539
C6	129.8115	C6	127.5651
C3	129.295	C3	125.7112
C4	54.373	C4	54.4277
C7	39.3291	C8	40.0893
C8	36.977	C7	38.4019
C19	23.7906	C18	24.2097
C22	14.3645	C21	14.9906
		C27	162.7688

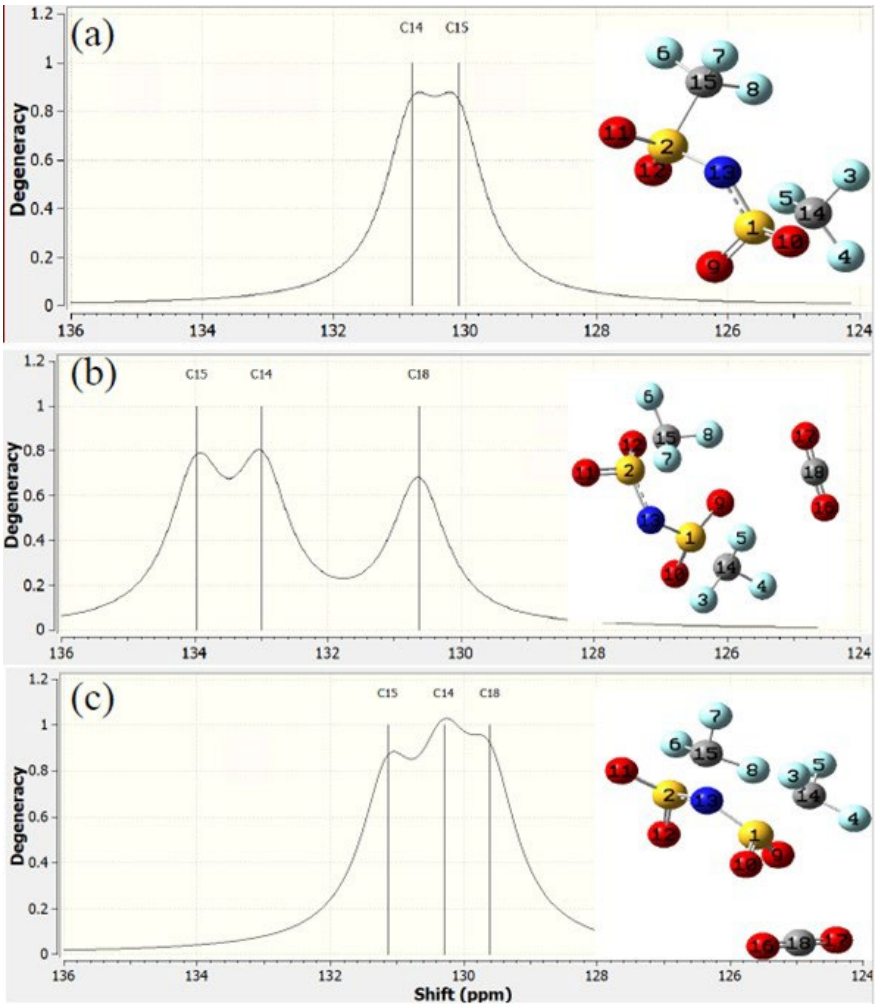

Figure S14. Comparison of simulated ^{13}C NMR spectra for (a) bis(trifluoromethylsulfonyl)imide (NTf_2), and the interaction of CO_2 with NTf_2 at (b) site A (NTf_2 + CO_2_A) and (c) site B (NTf_2 + CO_2_B). Atom colors: red = O, grey = C, white = H, blue = N, cyan = S.

Table S7. A comparison of chemical shifts of ^{13}C NMR

NTf2		**NTf2+CO2_A**		**NTf2+CO2_B**	
Atoms	**δ_calc (ppm)**	**Atoms**	**δ_calc (ppm)**	**Atoms**	**δ_calc (ppm)**
C15	130.117	C15	133.964	C15	131.136
C14	130.813	C14	132.9895	C14	130.2924
		C18	130.6304	C18	129.6061

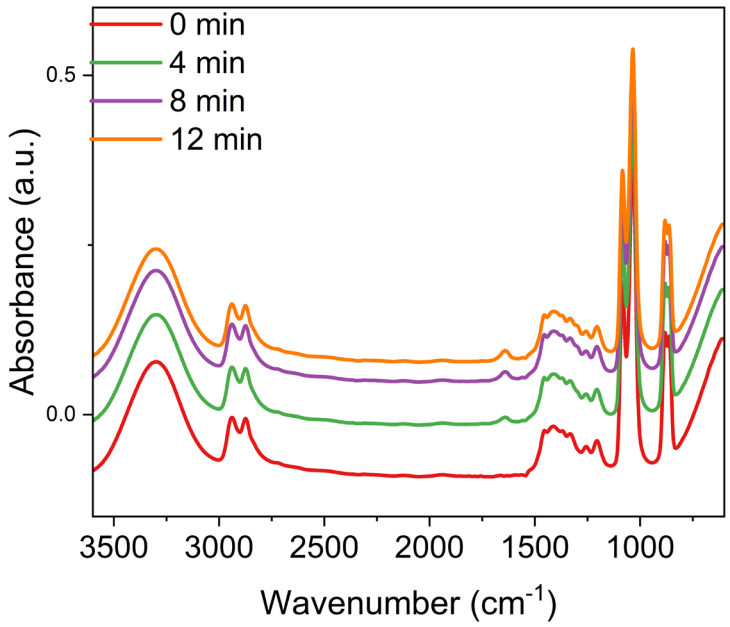

Figure S15. FTIR spectra of the DES system without IL at different time intervals.

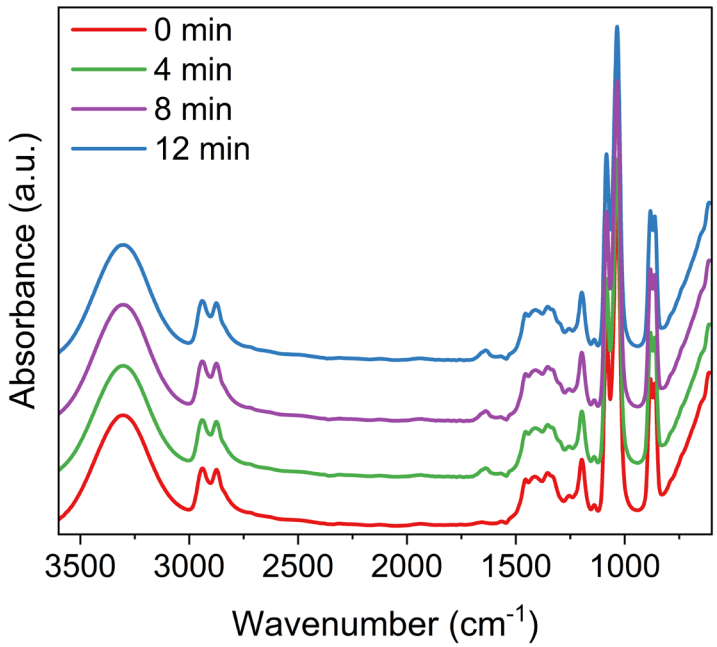

Figure S16. FTIR spectra of the DES system with IL at different time intervals.

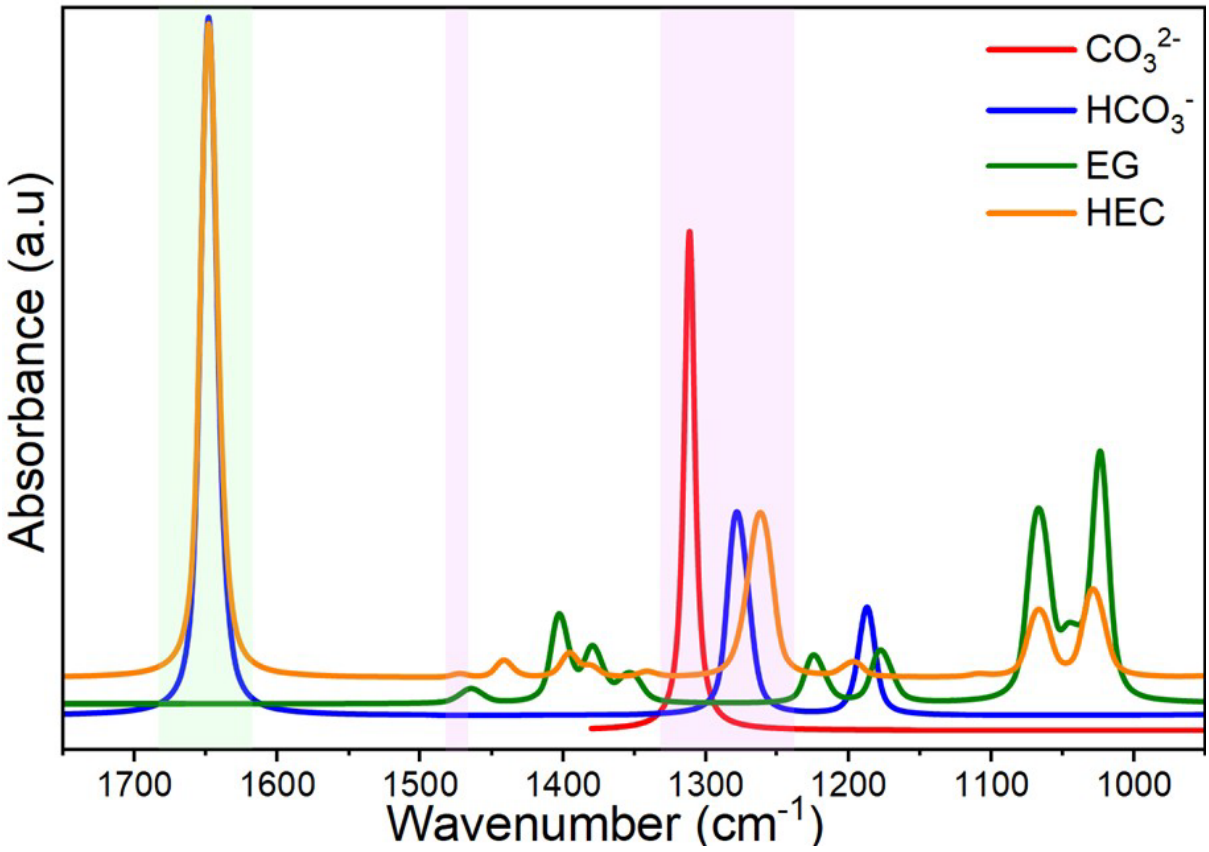

Figure S17. Comparison of simulated IR spectra of (a) carbonate (CO_3^{2-}), (b) bicarbonate (HCO_3^-), (c) ethylene glycol (EG), and (d) hydroxyethyl carbonate (HEC).

S2. Mathematical Modeling of IL-KOH kinetics

S2.1. Chemical Reactions

Based on the results observed from NMR and FTIR studies, chemisorption of CO_2 with alkaline DES can be elucidated in the following steps, as described in equations S1 to S5 rewritten in acidic form. The dissociation constants for equations S1 to S5 are roughly estimated from already published literature. [17, 18]

$$CO_2 + H_2O \underset{}{\overset{K_1}{\rightleftharpoons}} HCO_3^- + H^+; K_1 = 10^{-7.7} \quad \text{S1}$$

$$C_2O_2H_6 \underset{}{\overset{K_2}{\rightleftharpoons}} C_2O_2H_5^- + H^+; K_2 = 10^{-18.1} \quad \text{S2}$$

$$H_2O \underset{}{\overset{K_3}{\rightleftharpoons}} H^+ + OH^-; K_3 = 10^{-14} \quad \text{S3}$$

$$C_2O_2H_5^- + CO_2 \underset{}{\overset{K_4}{\rightleftharpoons}} C_2O_2H_5CO_2^-; K_4 = 10^{-15} \quad \text{S4}$$

$$HCO_3^- \underset{}{\overset{K_5}{\rightleftharpoons}} CO_3^{2-} + H^+; K_5 = 10^{-15.25} \quad \text{S5}$$

Rewriting equations S1 to S5 in terms of the dissociation constants gives equations S6 to S10.

$$K_3 = \frac{[H^+][OH^-]}{[H_2O]} \Rightarrow [H_2O] = \frac{[H^+][OH^-]}{K_3} \quad \text{S6}$$

$$K_1 = \frac{[HCO_3^-][H^+]}{[CO_2][H_2O]} \Rightarrow [HCO_3^-] = \frac{K_1[CO_2][H_2O]}{[H^+]} \Rightarrow [HCO_3^-] = \frac{K_1[CO_2][OH^-]}{K_3} \quad \text{S7}$$

$$K_2 = \frac{[C_2O_2H_5^-][H^+]}{[C_2O_2H_6]} \Rightarrow [C_2O_2H_5^-] = \frac{K_2[C_2O_2H_6]}{[H^+]} \quad \text{S8}$$

$$K_4 = \frac{[C_2O_2H_5CO_2^-]}{[C_2O_2H_5^-][CO_2]} \Rightarrow [C_2O_2H_5CO_2^-] = K_4[C_2O_2H_5^-][CO_2]$$
$$\Rightarrow [C_2O_2H_5CO_2^-] = \frac{K_4K_2[C_2O_2H_6][CO_2]}{[H^+]} \quad \text{S9}$$

$$K_5 = \frac{[CO_3^{2-}][H^+]}{[HCO_3^-]} \Rightarrow [CO_3^{2-}] = \frac{K_5[HCO_3^-]}{[H^+]} = \frac{K_5K_1[CO_2][OH^-]}{[H^+]K_3} \quad \text{S10}$$

S2.2. Conservation of Ethylene Glycol

To understand the variation of species, based on the change in concentration of hydroxide in the alkaline DES, additional constraints are imposed. By conserving the initial and final concentration of ethylene glycol, one can write:

$$[C_2O_2H_6]_0 = [C_2O_2H_6] + [C_2O_2H_5^-] + [C_2O_2H_5CO_2^-] \quad \text{S11}$$

Rearranging the equation S11 and substituting the values obtained earlier, we can write:

$$\frac{[C_2O_2H_5^-][H^+]}{K_2} = [C_2O_2H_6]_0 - [C_2O_2H_5^-] - K_4[C_2O_2H_5^-][CO_2] \quad \text{S12}$$

Further rearrangement gives equation S13

$$[C_2O_2H_5^-]\left(\frac{[H^+]}{K_2} + 1 + K_4[CO_2]\right) = [C_2O_2H_6]_0$$

$$\Rightarrow [C_2O_2H_5^-] = \frac{[C_2O_2H_6]_0}{\frac{[H^+]}{K_2} + 1 + K_4[CO_2]} \Rightarrow [C_2O_2H_5^-] = \frac{K_2[C_2O_2H_6]_0}{[H^+] + K_2 + K_2K_4[CO_2]} \quad \text{S13}$$

Thus, equation S9 can be written in terms of the initial concentration of CO_2 and initial concentration of EG, i.e. $[C_2O_2H_6]_0$, as follows:

$$[C_2O_2H_5CO_2^-] = \frac{K_4K_2[C_2O_2H_6]_0[CO_2]}{[H^+] + K_2 + K_2K_4[CO_2]} \quad \text{S14}$$

S2.3. Conservation of charge

Similar to conservation equations for Section S1.2, for an electroneutral system, the number of cations should be equal to the number of anions as shown in equations S15 and S16.

$$[H^+] + [K^+] = [OH^-] + [HCO_3^-] + 2[CO_3^{2-}] + [C_2O_2H_5^-] + [C_2O_2H_5CO_2^-] \quad \text{S15}$$

Since the K^+ ions are just spectator ions in chemisorption of CO2 in alkaline DES, the concentration of K^+ is set to 0.1 M. Therefore, equation S15 can be rearranged and rewritten as :

$$[H^+] + 0.1 - [OH^-] - \frac{K_1[CO_2][OH^-]}{K_3} \quad \text{S16}$$

$$-\frac{2K_5K_1[CO_2][OH^-]}{K_3[H^+]} - \frac{K_2[C_2O_2H_6]_0(1 + K_4[CO_2])}{[H^+] + K_2 + K_2K_4[CO_2]} = 0$$

S2.4. Conservation of protons

Since equation S16 has two unknown variables, i.e., H^+ and CO_2, the proton conservation equation has to be employed to reduce the degrees of freedom and determine all species in the chemisorption system.

Initial protons before the reaction = Final protons after the reaction

$$[C_2O_2H_6]_0 + [OH^-]_0 = [C_2O_2H_6] + [OH^-] + [HCO_3^-] + [H^+] + 2[H_2O] \quad \text{S17}$$

By substituting the initial concentration of EG, i.e. $[C_2O_2H_6]_0$ from equation S11, we obtain S18 as follows:

$$[C_2O_2H_6] + [C_2O_2H_5^-] + [C_2O_2H_5CO_2^-] + [OH^-]_0 \quad \text{S18}$$
$$= [C_2O_2H_6] + [OH^-] + [HCO_3^-] + [H^+] + 2[H_2O]$$

$$[C_2O_2H_5^-] + [C_2O_2H_5CO_2^-] + [OH^-]_0 - [OH^-] - [HCO_3^-] - [H^+] - 2[H_2O] = 0 \quad \text{S19}$$

$$\frac{K_2[C_2O_2H_6]_0(1+K_4[CO_2])}{[H^+]+K_2+K_2K_4[CO_2]}+0.1-[OH^-]-\frac{K_1[CO_2][OH^-]}{K_3}-[H^+]-\frac{2[H^+][OH^-]}{K_3}=0 \quad \text{S20}$$

Finally, by solving equations S16 and S20, the concentration of H^+ and CO_2 can be obtained at various concentrations of OH^- in the system. Concentration of the remaining species, such as CO_3^{2-}, $HCO3^-$, $C_2O_2H_5^-$, $C_2O_2H_5CO_2^-$, can be determined by substituting back the obtained values of H^+ and CO_2 in equations S6 to S10. Final values reported in the main manuscript are obtained from the OH^- concentrations of 0.092 to 1e-4 M. To quantify the reaction extent, each reaction (S1-S5) was assigned a corresponding variable ζ_1 to ζ_5.

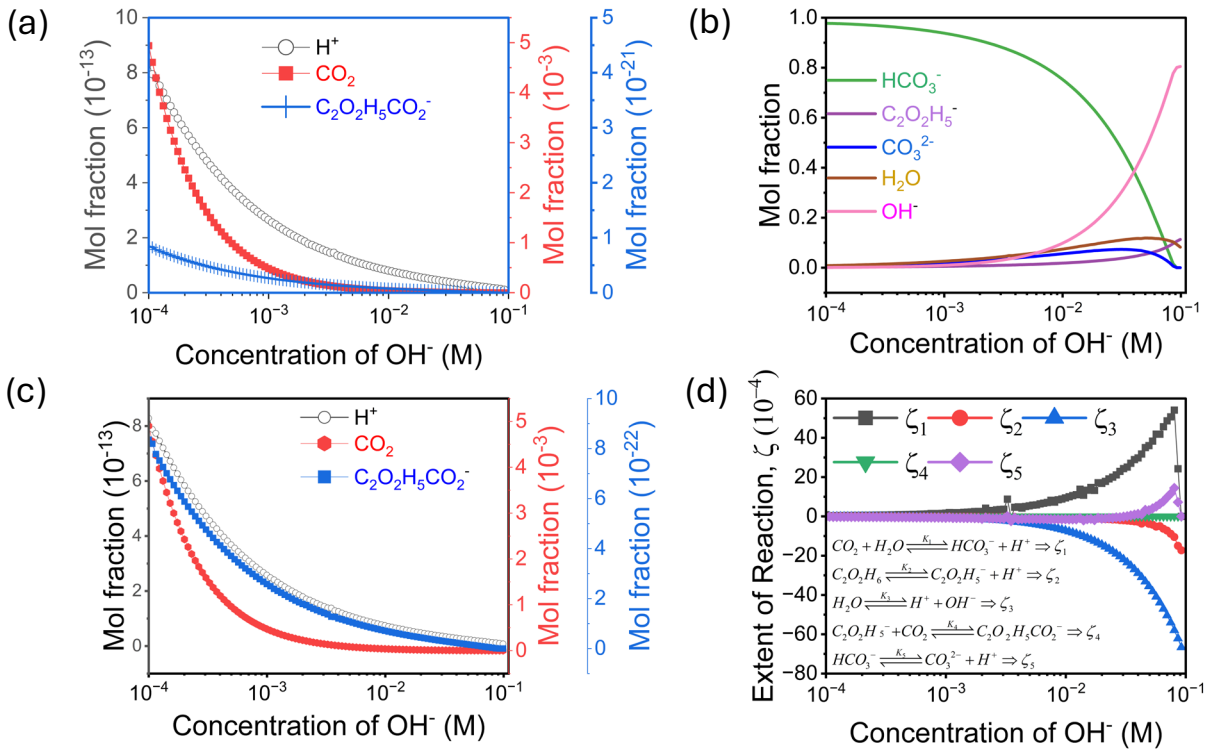

Figure S18. (a) Speciation diagram spanning various hydroxide concentrations of H^+ CO_2, $C_2O_2H_5CO_2^-$ without water being considered in mol fraction calculations. (b) Speciation diagram spanning various hydroxide concentrations, with water being considered in mol fraction calculations. (c)Speciation diagram spanning various hydroxide concentrations of H^+ CO_2, $C_2O_2H_5CO_2^-$ with water being considered in mol fraction calculations. (d) Extent of reaction spanning various hydroxide concentrations.

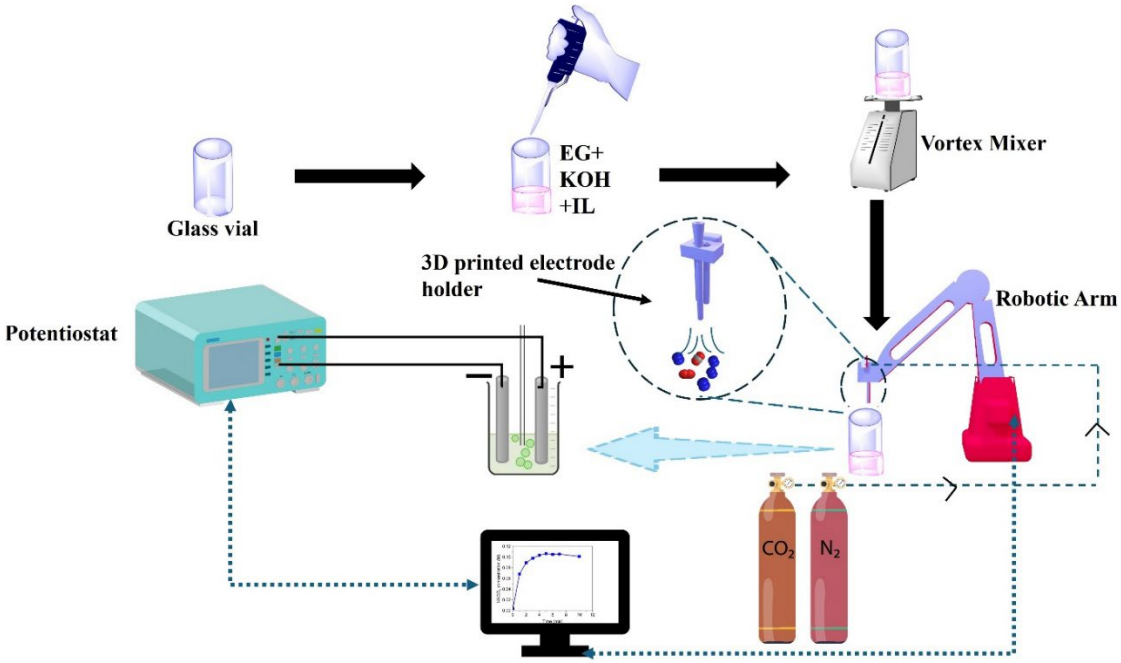

Figure S19. Schematic illustration of the system for evaluation of CO_2 capture kinetics in DES and DES-IL mixtures.

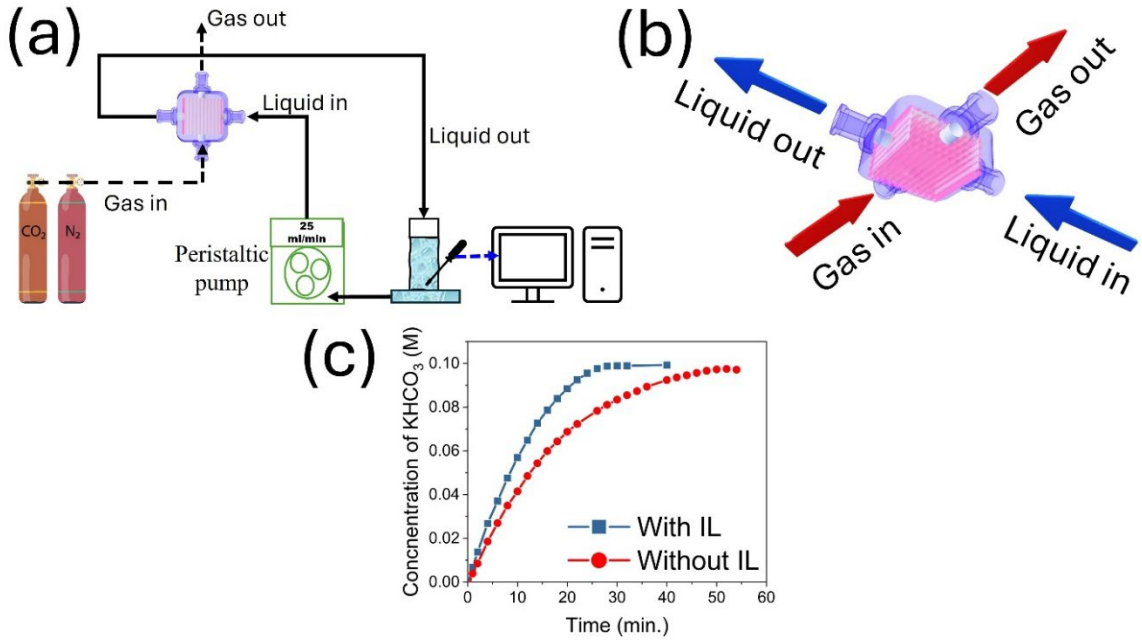

Figure S20. **(a)** CO_2 chemisorption experiments in 3M® Hollow Fiber module **(b)** 3D view of 3M® Hollow Fiber module **(c)** timed study of KOH conversion in the presence of IL and without IL. IL is BMIM NTf_2 at a mixed volume percentage of 5%. All experiments were conducted at 298 K, with an initial concentration of 0.1 M KOH to compare the influence of IL. The feed gas consists of 10% CO_2, and the balance is N_2 gas.

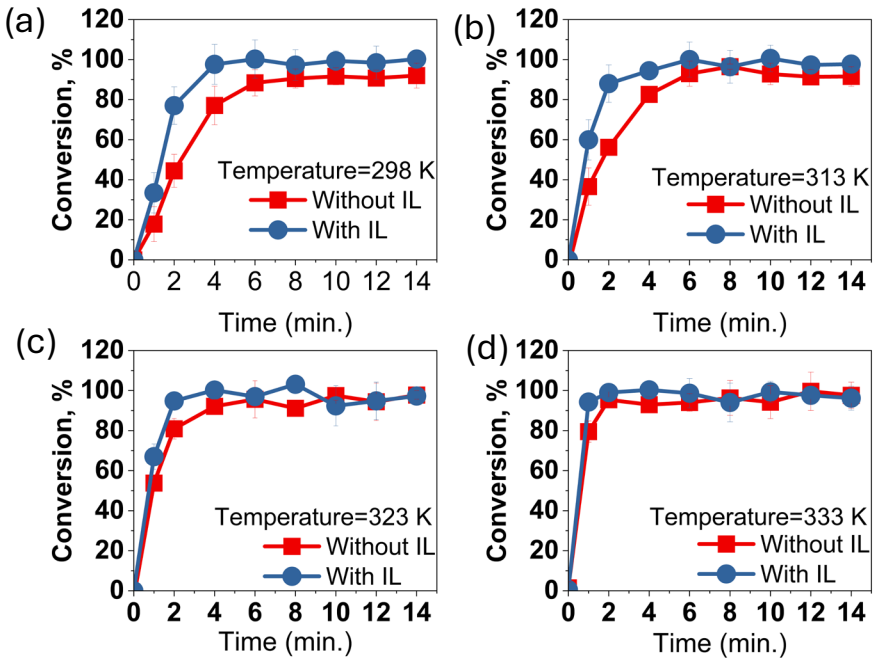

Figure S21. Time-dependent hydroxide conversion with and without IL at temperatures (a) 298 K, (b) 313 K, (c) 323 K, (d) 333 K. IL is BMIM NTf_2 at a mixed volume percentage of 5%. All experiments were conducted at 298 K, with an initial concentration of 0.1 M KOH to compare the influence of IL. The feed gas consists of 10% CO_2, and the balance is N_2 gas.

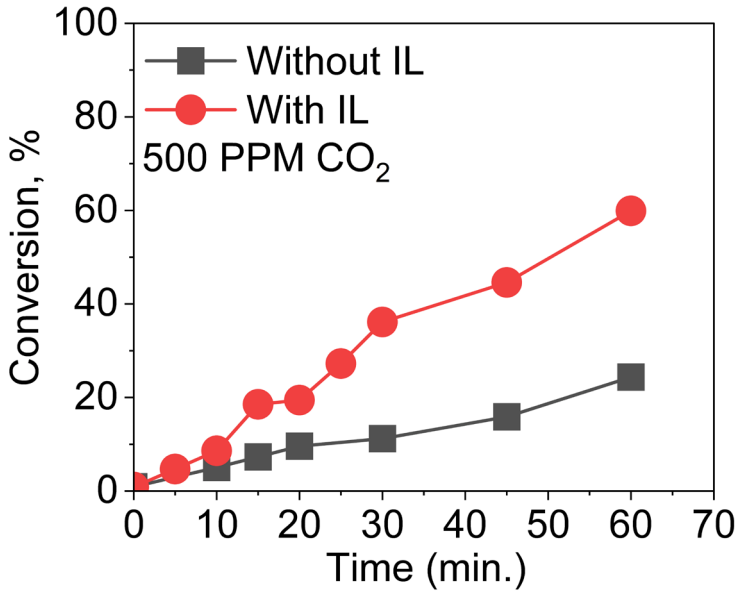

Figure S22. Time-dependent hydroxide conversion in the presence of IL and without IL. IL is BMIM NTf_2 at a mixed volume percentage of 5%. All experiments were conducted at 298 K, with an initial concentration of 0.1 M KOH to compare the influence of IL. The feed gas consists of 500 PPM CO_2, and the balance is N_2 gas.

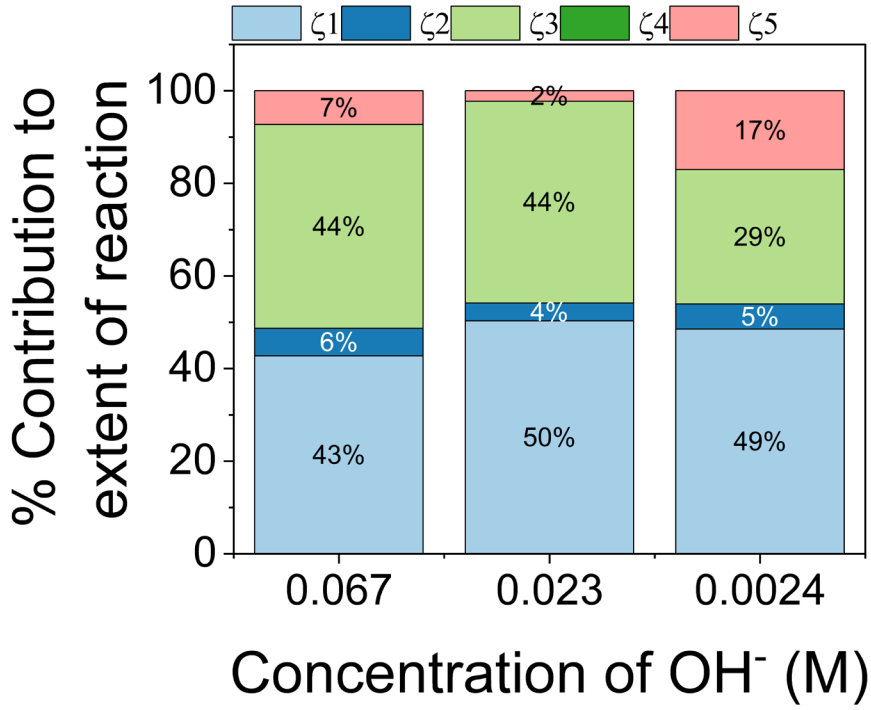

Figure S23. Comparison of various percentages of contribution to the extent of reaction based on the magnitude at different concentrations of OH- concentration.

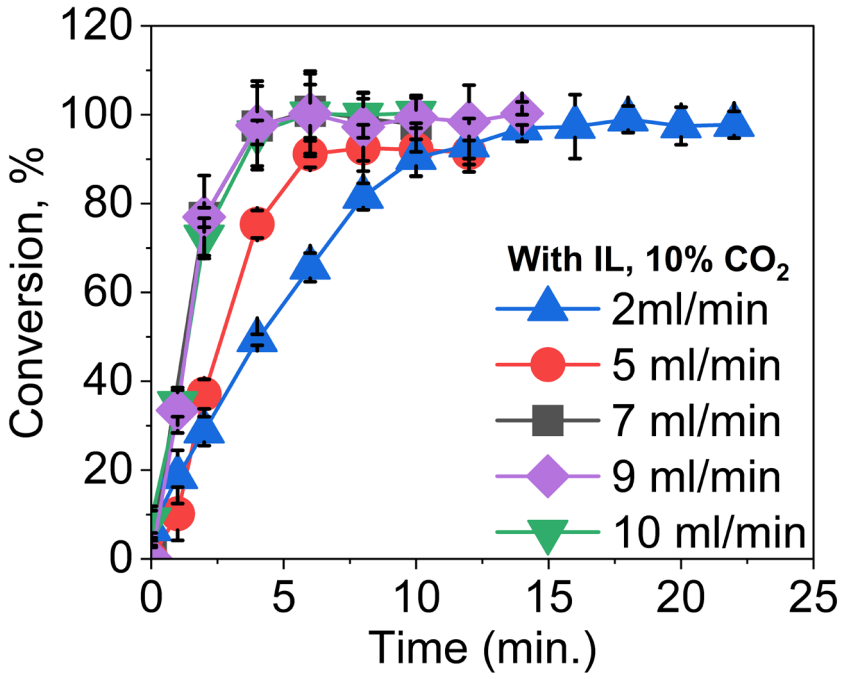

Figure S24. Time-dependent hydroxide conversion in the presence of IL at the different flow rates. IL is BMIM NTf_2 at a mixed volume percentage of 5%. All experiments were conducted at 298 K, with an initial concentration of 0.1 M KOH to compare the influence of IL. The feed gas consists of 10% CO_2, and the balance is N_2 gas.

Table S8. List of ILs, and their corresponding volume percentage, concentration, mol fraction, and pseudo 1st order constants used in the experiment. All experiments were conducted at atmospheric pressure.

Sample Name	IL volume percentage, %	Concentration of IL, M	Mol fraction	Temperature, K	k, (min^{-1})	Error	R^2
No IL	-	-	-	298	0.29	0.06	0.96
EMIM NTF2	5	0.19	0.01	298	0.52	0.03	0.97
EMIM OTf	5	0.27	0.02	298	0.53	0.04	0.95
BMIM DCA	5	0.26	0.01	298	0.77	0.02	0.99
BMIM OTf	5	0.23	0.01	298	1.18	0.1	0.98
BMIM PF6	5	0.24	0.01	298	0.38	0.07	0.91
BMIM NTF2	5	0.17	0.01	298	0.733	0.19	0.94
BMIM I	5	0.28	0.02	298	1.26	0.05	0.99
HMIM OTf	5	0.20	0.01	298	0.93	0.13	0.94
HMIM NTF2	5	0.15	0.01	298	0.83	0.12	0.93
HMIM I	5	0.25	0.01	298	0.78	0.05	0.99
HMIM PF6	5	0.21	0.01	298	0.7	0.02	0.99
EMIM NTF2	10	0.38	0.02	298	0.67	0.03	0.98
EMIM NTF2	20	0.76	0.05	298	0.18	0.02	0.93
BMIM NTF2	10	0.34	0.02	298	0.24	0.01	0.97
BMIM NTF2	20	0.68	0.05	298	0.15	0.01	0.97
HMIM NTF2	10	0.30	0.02	298	0.21	0.02	0.96
HMIM NTF2	20	0.60	0.04	298	0.087	0.003	0.98
BMIM NTF2	5	0.19	0.01	313	1.06	0.08	0.99
BMIM NTF2	5	0.19	0.01	323	1.48	0.21	0.98
BMIM NTF2	5	0.19	0.01	333	2.3	0.32	0.98
No IL	5	-	-	313	0.43	0.035	0.96
No IL	5	-	-	323	0.84	0.022	0.99
No IL	5	-	-	333	1.53	0.021	0.99

Table S9 Activation parameters from Eyring analysis for CO_2 chemisorption in absence and presence of BMIM NTF2 at specified mol fraction.

IL mol fraction, χ_{IL}	ΔH, kJ/mol	ΔS, J/mol/K
0	36.73	-201.14
0.01	23.91	-235.85

S3. Nonlinear fitting of the effect of the concentration of IL on CO_2 chemisorption

S3.1. Chemical Reactions

Chemisorption of CO_2 in the presence of DES-IL systems can be explained by considering the chemical reaction as a two-step reaction. A similar treatment of the reaction system is commonly found in the Michaelis-Menten reaction.[19, 20] Equation S21 can be considered as a reversible reaction with pseudo-steady state approximation (PSSA). The association and dissociation of IL with hydroxide ion are determined by rate constants k_1 and k_{-1}.

$$IL + CO_2(l) \underset{k_{-1}}{\overset{k_1}{\rightleftharpoons}} ILCO_2 \quad \text{S21}$$

After the formation of $ILOH^-$, the reaction proceeds with the CO_2 dissolved in the liquid as shown in equation S22.

$$ILCO_2 + OH^- \xrightarrow{k_2} ILHCO_3^- \quad \text{S22}$$

Rewriting the equation S21 in the differential form, we obtain:

$$\frac{dc_{ILCO_2}}{dt} = k_1 c_{IL} c_{CO_2(l)} - k_2 c_{ILCO_2} c_{OH^-} - k_{-1} c_{ILCO_2} \quad \text{S23}$$

Invoking PSSA, S23 equation achieves steady state rapidly, and leads to :

$$0 = k_1 c_{IL} c_{CO_2(l)} - k_2 c_{ILCO_2} c_{OH^-} - k_{-1} c_{ILCO_2} \quad \text{S24}$$

S3.2. Conservation of Ionic Liquid

To determine C_{ILOH} we invoke conservation of ionic liquid before and after the chemisorption reactions as shown in equation S25

$$c_{IL_o} = c_{IL} + c_{ILCO_2} \Rightarrow c_{IL} = c_{IL_o} - c_{ILCO_2} \quad \text{S25}$$

Replacing the initial IL concentration, i.e. $C_{IL0,}$ in equation S24, we obtain:

$$k_1 c_{IL_o} c_{CO_2(l)} - k_1 c_{ILCO_2} c_{CO_2(l)} - k_2 c_{ILCO_2} c_{OH^-} - k_{-1} c_{ILCO_2} = 0 \quad \text{S26}$$

Rearranging terms, we obtain C_{ILOH} as shown in equation S27.

$$c_{ILCO_2} = \frac{k_1 c_{IL_o} c_{CO_2(l)}}{k_1 c_{CO_2(l)} + k_2 c_{OH^-} + k_{-1}} \quad \text{S27}$$

S3.3. Modelling of IL over the interface

Since ILs are composed of long hydrophobic chain molecules, we know that ILs prefer to align along the air-solvent interface, as shown in **Figure S25,** mimicking surfactant-like behavior.[21-23] So, to mathematically model the presence of IL along the air-liquid interface, in the form of the Langmuir-Adsorption isotherm in combination with the Szyszkowski–Langmuir equation as shown in equation S28.

$$\gamma = \gamma_0 - A\ln(1 + Kc_{IL_o}) \quad \text{S28}$$

where γ is the surface tension of the solvent, γ_0 is the surface tension of pure alkaline DES, A is a proportionality constant, K is the Langmuir constant. Surface tension data for different volume percentages of IL in DES were determined using a tensiometer. Additional details can be found in Section S1.7.

Furthermore, the Langmuir-type surface coverage is given by

$$\theta = \frac{Kc_{IL_o}}{1 + Kc_{IL_o}} \quad \text{S29}$$

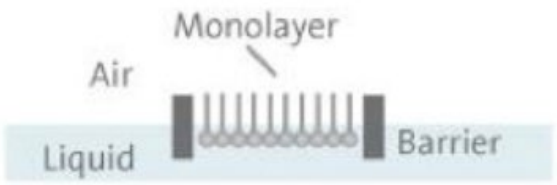

Figure S25. Schematic for ionic liquid alignment at the air-liquid interface.

S3.4. Coupled mass transfer reactions

The bubble theory for reaction, coupled with mass transfer, explains the interplay between chemical reactions taking place at or near the surface of a rising gas bubble and the movement of reactants and products between the bubble and the surrounding liquid.[24] This concept is fundamental in multiphase reactor engineering and is particularly important in gas–liquid systems like absorption columns, bubble columns, and fermenters. [25, 26]

Balancing two driving forces across a bubble

$$ak_l^{eff}(c_{CO_2(s)} - c_{CO_2(l)}) = k_2 c_{OH^-} c_{ILCO_2} \quad \text{S30}$$

Where a is the interfacial area of the bubble, $C_{CO2(S)}$ is the saturated concentration of CO_2 in the gas phase, $C_{CO2(l)}$ is the CO_2 concentration in the liquid phase, and k_2 is the reaction rate constant from equation S22. Furthermore, k_l^{eff} is the effective mass transfer coefficient as shown in equation S31

$$ak_l^{eff} = a(\theta k_l^{IL} + (1-\theta)k_l^{EG}) \quad \text{S31}$$

Rearranging and substituting the terms from equation S27 in S31 gives equation S32

$$ak_l^{eff} c_{CO_2(s)} = ak_l^{eff} c_{CO_2(l)} + \frac{k_2 c_{OH^-} k_1 c_{IL_o} c_{CO_2(l)}}{k_1 c_{CO_2(l)} + k_2 c_{OH^-} + k_{-1}} \quad \text{S32}$$

Now, equation S22 can be rewritten in differential form to obtain the concentration of $ILHCO_3^-$ complex.

$$\frac{dc_{ILHCO_3^-}}{dt} = \frac{k_2 c_{OH^-} k_1 c_{IL_o} c_{CO_2(l)}}{k_1 c_{CO_2(l)} + k_2 c_{OH^-} + k_{-1}} \quad \text{S33}$$

Furthermore, it can be assumed initial concentration of hydroxide is equal to the sum of the concentration of hydroxide at any time and the bicarbonate formed, so:

$$c^o_{OH^-} \approx c_{OH^-} + c_{ILHCO_3^-} \Rightarrow c_{OH} \approx 0.1 - c_{ILHCO_3^-} \quad \text{S34}$$

Substituting the terms obtained from equation S34 in S33 and S32 leads to equations S35 and S36

$$\frac{dc_{ILHCO_3^-}}{dt} = \frac{k_2 k_1 c_{IL_o} (0.1 - c_{ILHCO_3^-}) c_{CO_2(l)}}{k_2 (0.1 - c_{ILHCO_3^-}) + k_{-1} + k_1 c_{CO_2(l)}} \quad \text{S35}$$

$$ak_l^{eff} c_{CO_2(s)} = ak_l^{eff} c_{CO_2(l)} + \frac{k_2 k_1 c_{IL_o} c_{CO_2(l)} (0.1 - c_{ILHCO_3^-})}{k_1 c_{CO_2(l)} + k_2 (0.1 - c_{ILHCO_3^-}) + k_{-1}} \quad \text{S36}$$

Thus, equations S35 and S36 can be simultaneously fit to different IL concentrations to determine the unknown parameters such as k_1, k_{-1}, a, and k_2 for the alkaline IL-DES system. Simulations required for fitting were performed using **MATLAB R2024b** to model the system's dynamic behavior.

Table S10. List of parameters obtained after fitting with the experimental data.

Constants	Description, units	BMIM NTf2	HMIM NTf2
k_1	Rate constant, L $mol^{-1}s^{-1}$	61.5	63.5
k_2	Rate constant, s^{-1}	0.35	0.31
k_{-1}	Rate constant, L $mol^{-1}s^{-1}$	2.14E-02	2.47E-02
k_l^{IL}	Mass Transfer Coeffecient of Ionic liquid, ms^{-1}	9.70E-06	9.70E-06
k_l^{EG}	Mass Transfer Coeffecient of Ethylene Glycol-KOH solution, ms^{-1}	1.01E-02	1.01E-02
$a_{5\%}$	Interfacial surface area, m^2/m^3	703	1600
$a_{10\%}$	Interfacial surface area of 10 vol% mixture, m^2/m^3	423	1290
$a_{20\%}$	Interfacial surface area of 20 vol% mixture, m^2/m^3	403	1200
K	Langmuir Constant	21	120
$C_{CO2}(s)$	Saturated Concentration of CO2 on gas side	4.00E-04	4.00E-04

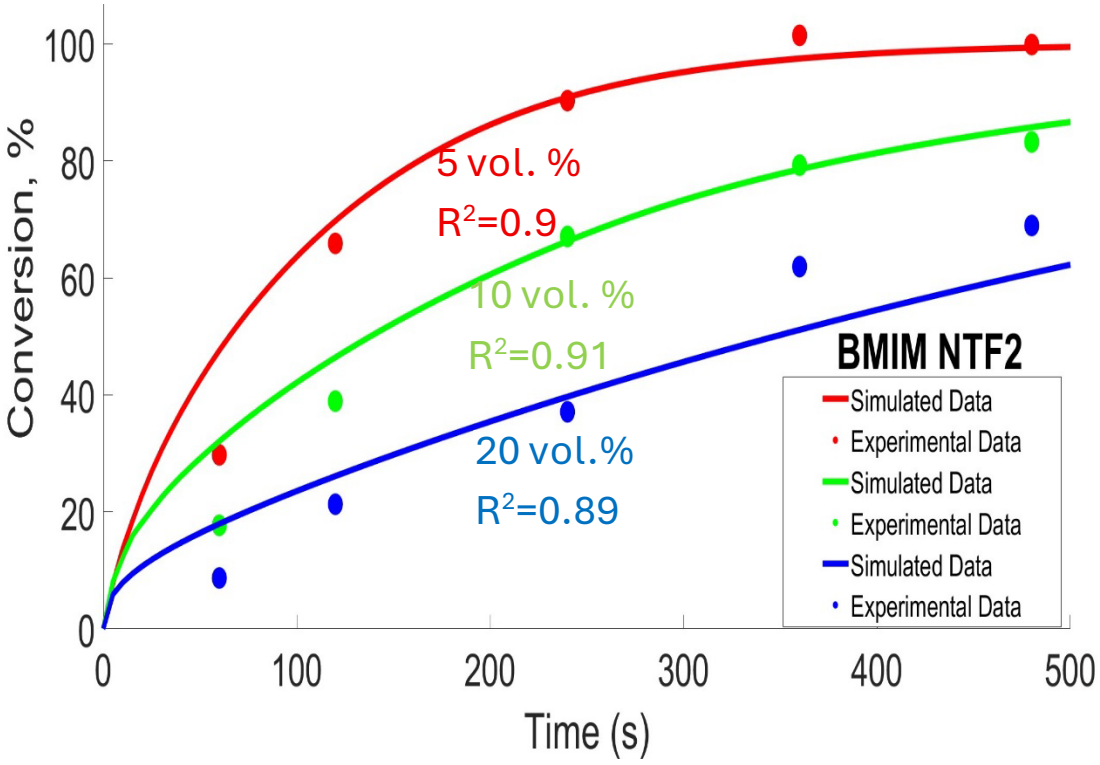

Figure S26. Comparison of experimental data with simulated data for the impact of volume percentage of BMIM NTf_2 on CO_2 chemisorption.

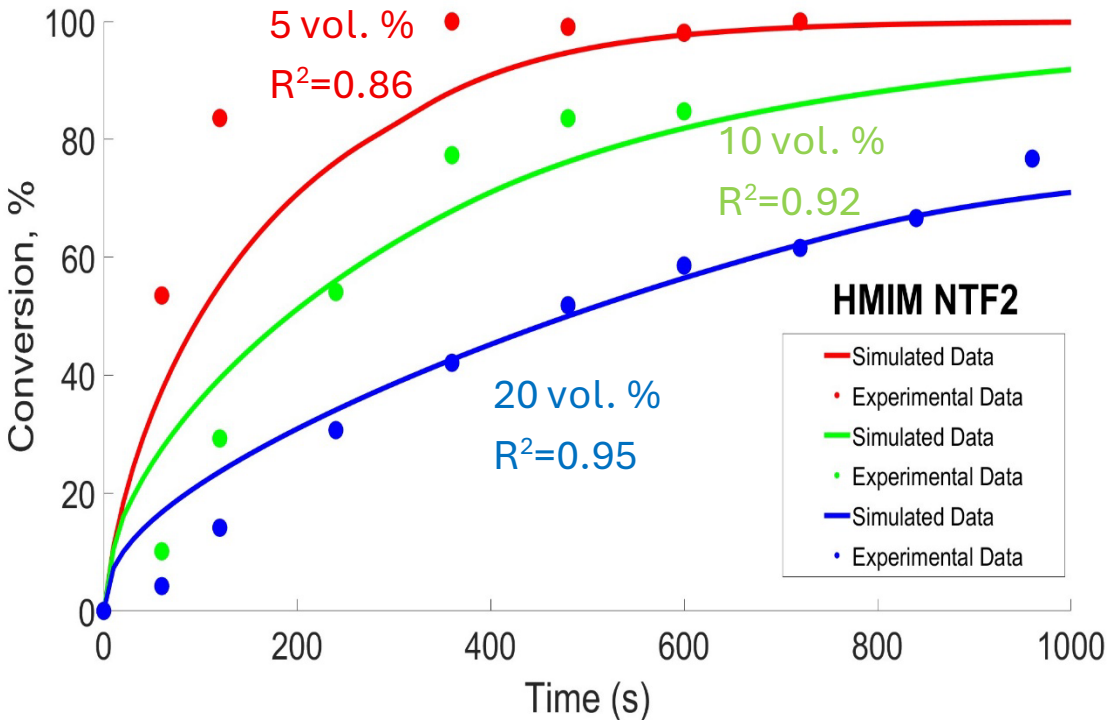

Figure S27. Comparison of experimental data with simulated data for the impact of volume percentage of HMIM NTf_2 on CO_2 chemisorption.

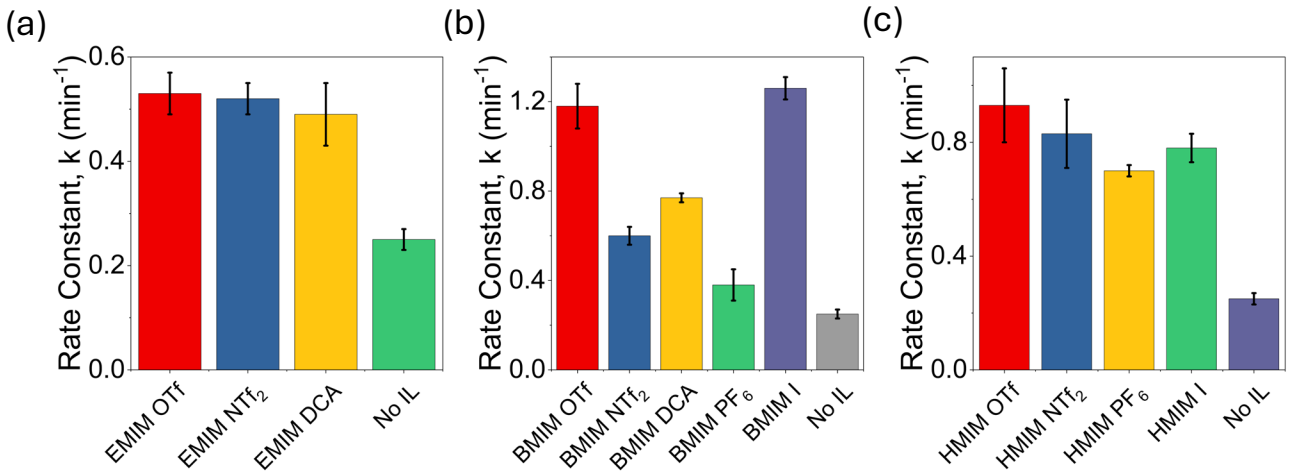

Figure S28. Pseudo first-order rate constants of CO_2 chemisorption for (a) EMIM, (b) BMIM, and (c) HMIM-based ILs. The feed gas consists of 10% CO_2, and the balance is N_2 gas.

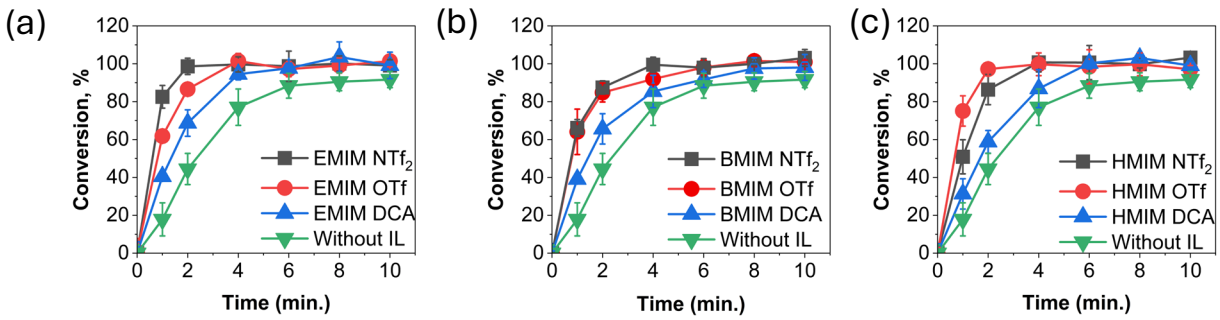

Figure S29. **:** Time-dependent hydroxide conversion in the presence of **(a)** EMIM-based ILs, **(b)** BMIM-based ILs, and **(c)** HMIM-based ILs. All experiments were conducted at 298 K, 0.1 M concentration of IL, and an initial concentration of 0.1 M KOH to compare the influence of IL cation and anion structure on conversion rates. The feed gas consists of 10% CO_2, and the balance is N_2 gas.

References

(1) Chauhan, R.; Sartape, R.; Mishra, R.; Shah, J. K.; Singh, M. R. High-throughput measurements of CO2 permeance and solubility in ionic liquid reveal a synergistic role of ionic interactions and void fractions. *Chemical Engineering Journal* **2024**, *496*, 153697.
(2) Brinkmann, F.; Dam, N. E.; Deák, E.; Durbiano, F.; Ferrara, E.; Fűkő, J.; Jensen, H. D.; Máriássy, M.; Shreiner, R. H.; Spitzer, P. Primary methods for the measurement of electrolytic conductivity. *Accreditation and quality assurance* **2003**, *8*, 346-353.
(3) Jarosik, A.; Krajewski, S. R.; Lewandowski, A.; Radzimski, P. Conductivity of ionic liquids in mixtures. *Journal of Molecular Liquids* **2006**, *123* (1), 43-50.
(4) Sartape, R.; Prajapati, A.; Kani, N. C.; Rojas, T.; Dandu, N. K.; Dhakal, P.; Thorat, A. S.; Xie, J.; Bessa, I.; Galante, M. T. Reply to the 'Comment on "Migration-assisted, moisture gradient process for ultrafast, continuous CO 2 capture from dilute sources at ambient conditions"'by J. Casado, Energy Environ. Sci., 2022, 10.1039/D2EE00555G. *Energy & Environmental Science* **2022**, *15* (9), 3994-3996.
(5) Prajapati, A.; Sartape, R.; Rojas, T.; Dandu, N. K.; Dhakal, P.; Thorat, A. S.; Xie, J.; Bessa, I.; Galante, M. T.; Andrade, M. H. Migration-assisted, moisture gradient process for ultrafast, continuous CO 2 capture from dilute sources at ambient conditions. *Energy & Environmental Science* **2022**, *15* (2), 680-692.
(6) Frisch, M.; Trucks, G.; Schlegel, H.; Scuseria, G.; Robb, M.; Cheeseman, J.; Scalmani, G.; Barone, V.; Petersson, G.; Nakatsuji, H. Gaussian 16, revision a. 03, gaussian, inc., wallingford ct. *Gaussian16 (Revision A. 03)* **2016**.
(7) Becke, A. D. Density-functional thermochemistry. III. The role of exact exchange. *The Journal of chemical physics* **1993**, *98* (7), 5648-5652.
(8) Grimme, S.; Antony, J.; Ehrlich, S.; Krieg, H. A consistent and accurate ab initio parametrization of density functional dispersion correction (DFT-D) for the 94 elements H-Pu. *The Journal of chemical physics* **2010**, *132* (15).
(9) Grimme, S.; Ehrlich, S.; Goerigk, L. Effect of the damping function in dispersion corrected density functional theory. *Journal of computational chemistry* **2011**, *32* (7), 1456-1465.
(10) Marenich, A. V.; Cramer, C. J.; Truhlar, D. G. Universal solvation model based on solute electron density and on a continuum model of the solvent defined by the bulk dielectric constant and atomic surface tensions. *The Journal of Physical Chemistry B* **2009**, *113* (18), 6378-6396.
(11) Ditchfield, R. Self-consistent perturbation theory of diamagnetism: I. A gauge-invariant LCAO method for NMR chemical shifts. *Molecular Physics* **1974**, *27* (4), 789-807.
(12) Wolinski, K.; Hinton, J. F.; Pulay, P. Efficient implementation of the gauge-independent atomic orbital method for NMR chemical shift calculations. *Journal of the American Chemical Society* **1990**, *112* (23), 8251-8260.
(13) Cheeseman, J. R.; Trucks, G. W.; Keith, T. A.; Frisch, M. J. A comparison of models for calculating nuclear magnetic resonance shielding tensors. *The Journal of chemical physics* **1996**, *104* (14), 5497-5509.
(14) Yoshida, H.; Takeda, K.; Okamura, J.; Ehara, A.; Matsuura, H. A new approach to vibrational analysis of large molecules by density functional theory: wavenumber-linear scaling method. *The Journal of Physical Chemistry A* **2002**, *106* (14), 3580-3586.
(15) Merrick, J. P.; Moran, D.; Radom, L. An evaluation of harmonic vibrational frequency scale factors. *The Journal of Physical Chemistry A* **2007**, *111* (45), 11683-11700.

(16) Andersson, M. P.; Uvdal, P. New scale factors for harmonic vibrational frequencies using the B3LYP density functional method with the triple-ζ basis set 6-311+ G (d, p). *The Journal of Physical Chemistry A* **2005**, *109* (12), 2937-2941.
(17) Lobaccaro, P.; Singh, M. R.; Clark, E. L.; Kwon, Y.; Bell, A. T.; Ager, J. W. Effects of temperature and gas–liquid mass transfer on the operation of small electrochemical cells for the quantitative evaluation of CO 2 reduction electrocatalysts. *Physical Chemistry Chemical Physics* **2016**, *18* (38), 26777-26785.
(18) Ripin, D.; Evans, D. pKa's of Inorganic and Oxo-Acids, Organic Division of the ACS. 2023.
(19) Ainsworth, S. Michaelis-menten kinetics. In *Steady-state enzyme kinetics*, Springer, 1977; pp 43-73.
(20) Cornish-Bowden, A. One hundred years of Michaelis–Menten kinetics. *Perspectives in Science* **2015**, *4*, 3-9.
(21) Nandwani, S. K.; Malek, N. I.; Lad, V.; Chakraborty, M.; Gupta, S. Study on interfacial properties of Imidazolium ionic liquids as surfactant and their application in enhanced oil recovery. *Colloids and Surfaces A: Physicochemical and Engineering Aspects* **2017**, *516*, 383-393.
(22) Tourne-Peteilh, C.; Coasne, B.; In, M.; Brevet, D.; Devoisselle, J.-M.; Vioux, A.; Viau, L. Surfactant behavior of ionic liquids involving a drug: from molecular interactions to self-assembly. *Langmuir* **2014**, *30* (5), 1229-1238.
(23) Łuczak, J.; Hupka, J.; Thöming, J.; Jungnickel, C. Self-organization of imidazolium ionic liquids in aqueous solution. *Colloids and Surfaces A: Physicochemical and Engineering Aspects* **2008**, *329* (3), 125-133.
(24) Treybal, R. E. Mass transfer operations. *New York* **1980**, *466*, 493-497.
(25) Barker, J. J.; Treybal, R. E. Mass transfer coefficients for solids suspended in agitated liquids. *AIChE Journal* **1960**, *6* (2), 289-295.
(26) Heijnen, J.; Van't Riet, K. Mass transfer, mixing and heat transfer phenomena in low viscosity bubble column reactors. *The Chemical Engineering Journal* **1984**, *28* (2), B21-B42.